

Bioinspired “Skin” with Cooperative Thermo-Optical Effect for Daytime Radiative Cooling

Meng Yang, Weizhi Zou, Jing Guo, Zhenchao Qian, Heng Luo, Shijia Yang, Ning Zhao,* Lorenzo Pattelli,* Jian Xu,* and Diederik S. Wiersma



Cite This: *ACS Appl. Mater. Interfaces* 2020, 12, 25286–25293



Read Online

ACCESS |

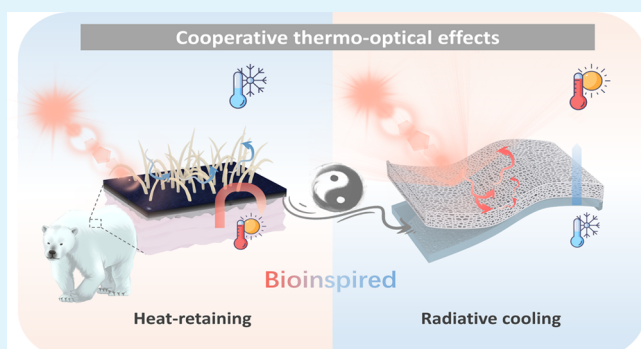
Metrics & More

Article Recommendations

Supporting Information

ABSTRACT: Energy-saving cooling materials with strong operability are desirable for sustainable thermal management. Inspired by the cooperative thermo-optical effect in the fur of a polar bear, we develop a flexible, superhydrophobic, and reusable cooling “skin” by laminating a poly(dimethylsiloxane) film with a highly scattering polyethylene aerogel. Owing to its high porosity (97.9%) and tailored pore size of $3.8 \pm 1.4 \mu\text{m}$, it can achieve superior solar reflectance ($\bar{R}_{\text{sun}} \sim 0.96$) and high transparency to irradiated thermal energy ($\bar{\tau}_{\text{PE,MIR}} \sim 0.8$) at a thickness of 2.7 mm. Combined with the low thermal conductivity ($0.032 \text{ W m}^{-1} \text{ K}^{-1}$) of the aerogel, the cooling skin exerts midday sub-ambient temperature drops of 5–6 °C in a metropolitan environment, with an estimated limit of 14 °C under ideal service conditions. Our generalized bilayer approach can be easily applied to different types of emitters, bridging the gap between night-time and daytime radiative cooling and paving the way for more cost-effective and scalable cooling materials.

KEYWORDS: aerogel, brightness, polar bear, radiative cooling, thermal insulation



INTRODUCTION

In recent years, high temperatures and extreme weather conditions are increasingly threatening human health and economy by inducing hyperthermia and material aging and even causing fires.^{1–3} To mitigate the negative effects of excessive heat, economical, scalable, and energy-saving cooling materials are desirable. In nature, living beings have developed efficient strategies harnessing both optical and thermal management to limit the consumption of internal energy.^{4–7} One prominent example is the polar bear, which uses its fur to retain body heat, thanks to a combination of radiative (transmitting a part of sunlight to warm the black skin while retaining MIR radiation from the body) and nonradiative mechanisms (thermal insulation from air convection) (Figure 1a-i).^{4,8–10} This raises an interesting question whether it is possible to design a flexible cooling “skin” exploiting this synergistic thermo-optical effect to achieve the opposite goal, i.e., to reflect solar energy and radiate heat to outer space through an atmospheric window (MIR, 8–13 μm wavelength) via the passive daytime radiative cooling (PDRC) approach.^{11,12}

Despite emerging breakthroughs in toughness, machinability, and scalability,^{12–15} PDRC devices still suffer from a limited range of suitable materials, modest cooling performance, and low operability. The strong dependence on spectral selectivity increases the difficulties to engineer the photonic

band gap of the emitters,^{16–18} ruling out most broad-band emitters capable of night-time cooling unless shielded from direct sunlight and the surrounding thermal radiation.^{19,20} With regards to other general ways to increase solar reflectance (\bar{R}_{sun}), metal coatings are easily corroded and lose efficacy rapidly, while large contents of white ceramic additives eventually degrade UV reflection, MIR radiation, and flexibility of cooling materials.^{3,13,21,22} Finally, even if ideal optical properties were fulfilled, PDRC efficiency is inevitably restrained by heat exchange with external air.^{14,20,23,24} To address this issue, high-porosity materials have been recently proposed to reduce parasitic heat gain, which are however still characterized by weak mechanical resistance and a limited emitter-independent scattering efficiency of sunlight.^{23,24}

Herein, we propose a bilayer approach combining a highly scattering layer of polyethylene (PE) nanoflake aerogel and a commercial poly(dimethylsiloxane) (PDMS) film laminated together to obtain a flexible cooling skin that can be used multiple times on various substrates (Figure 1a-ii). By

Received: February 29, 2020

Accepted: May 7, 2020

Published: May 7, 2020



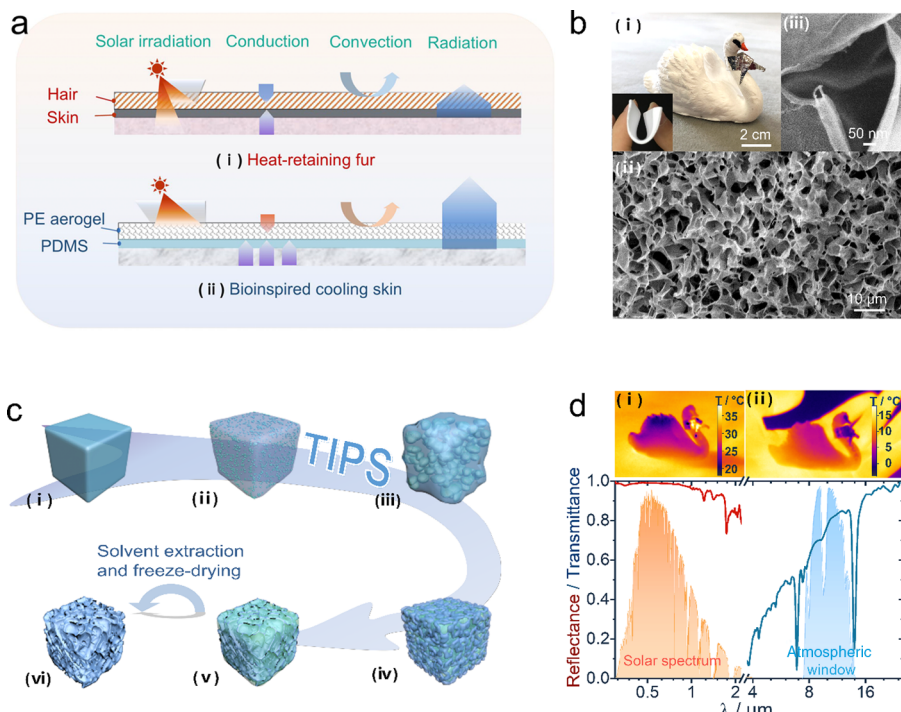


Figure 1. Bioinspired bilayer route using a highly scattering aerogel. (a) Schematic photothermal management of the heat-retaining fur of a polar bear (i) and bioinspired cooling skin with polyethylene (PE) aerogel of 97.9% porosity (ii, b–d). (b) Photographs of a swan-shaped aerogel decorated with multiwall carbon nanotubes coating (black), acrylic painting (orange), and aluminum foil stickers (silver) (i) and its morphology under a scanning electron microscope (SEM) (ii, iii); inset of (i) shows the aerogel flexibility. (c) Structural evolution during the preparation of aerogel: homogeneous PE/paraffin solution (i); island morphology induced by the precipitation and growth of paraffin-rich phase (ii, iii); bicontinuous networks of PE-rich and paraffin-rich phases (iv); gel physically cross-linked by the crystallization of PE (v); PE nanoflake network after paraffin removal by solvent extraction and freeze-drying (vi). (d) Spectrum of a 2.7 mm thick aerogel; insets show thermal images of the swan-shaped aerogel shot under direct sunlight outdoor (i) and held in hands indoor (ii).

optimizing its pore size distribution, we obtained a PE aerogel endowed with a high $\bar{R}_{\text{sun}} \sim 0.96$ and MIR transmittance ($\bar{\tau}_{\text{PE,MIR}} \sim 0.8$) at a thickness of just 2.7 mm, largely exceeding the scattering efficiency of other similar materials proposed for PDRC.^{3,24,25} In addition to the extreme low mass of PE (97.9% porosity), a tailored pore diameter (D_{pore}) of $3.8 \pm 1.4 \mu\text{m}$ contributes to enhancing the MIR transmission by favoring forward scattering through the whole atmospheric window. Finally, the PDRC efficiency of our PE/PDMS film is further improved, thanks to the thermal insulation provided by the aerogel (reaching a thermal conductivity as low as $32 \text{ mW m}^{-1} \text{ K}^{-1}$). As a result, we demonstrated a sub-ambient temperature reduction (ΔT_{cool}) of 5–6 °C measured at a solar irradiance (I_{sun}) $> 1000 \text{ W m}^{-2}$ in an urban area, with a calculated limit of 14 °C under ideal service conditions, which is comparative or superior to other reported results^{12–15,18–21,26,27} while allowing for a much broader freedom in the emitter selection. By taking advantage of the enhanced solar reflectance of the PE nanoflake aerogel and its cooperative thermo-optical effect, our approach opens a promising avenue for PDRC with enriched materials and strong operability under adverse service environments.

RESULTS AND DISCUSSION

In contrast to previous approaches based on bulk gelation or interface-mediated self-assembly,^{28,29} we have developed our PE nanoflake network (Figure 1b) starting from a bicontinuous structure comprising PE-rich and paraffin-rich phases via thermally induced phase separation (TIPS; Figure

1c and Supporting Information, Note 1). Tailoring the size and density of the pores formed after paraffin removal is the key to tune the thermo-optical properties of the final PE aerogel. Therefore, high-molecular-weight PE ($M_n \sim 4.5 \times 10^6$) and paraffin wax (melting temperature of 48–50 °C) are preferred to prepare aerogels for two reasons. First, the enormous kinetic asymmetry (difference in the mobility of PE and paraffin molecules) retards the phase growth of the bicontinuous structure, thus allowing smaller paraffin-rich phases to be retained before fixation by PE crystallization (Figure 1c–v).^{30,31} Second, using paraffin wax instead of more commonly used solvents such as liquid paraffin, leads to a gel with significantly superior machinability and dimensional stability (Supporting Information, Note 2).

Thanks to these improved structural stabilities, the as-prepared PE nanoflake networks can reach porosities as high as 99.4% (Supporting Information, Note 3), which are associated with a particularly low thermal conductivity varying accordingly in the range between 22 and $32 \text{ mW m}^{-1} \text{ K}^{-1}$. In the following, we consider a sample with 97.9% porosity, which shows excellent mechanical strength (compression modulus is $0.72 \pm 0.05 \text{ MPa}$; Figure S9) as well as high reflectance against solar irradiation ($\bar{R}_{\text{sun}} \sim 0.96$) and transparency through the atmospheric window ($\bar{\tau}_{\text{PE,MIR}} \sim 0.8$) (Figure 1d). These properties are qualitatively illustrated in Figure 1d, which shows a swan-shaped aerogel at a lower temperature than the background fabric under direct sunlight (Figure 1d-i), and its transparency to MIR radiating from a human hand at room temperature (Figure 1d-ii).

To date, modulating polymer-based structures to achieve sufficient \bar{R}_{sun} remains particularly challenging, especially when the filling ratio (f) of PE must be constrained to ensure a high $\bar{\tau}_{\text{PE,MIR}}$.^{3,24,25} We found that the structures of PE aerogels are rather sensitive to the initial polymer concentration (1–4 wt %) (Figure 2a and Supporting Information, Note 3), changing

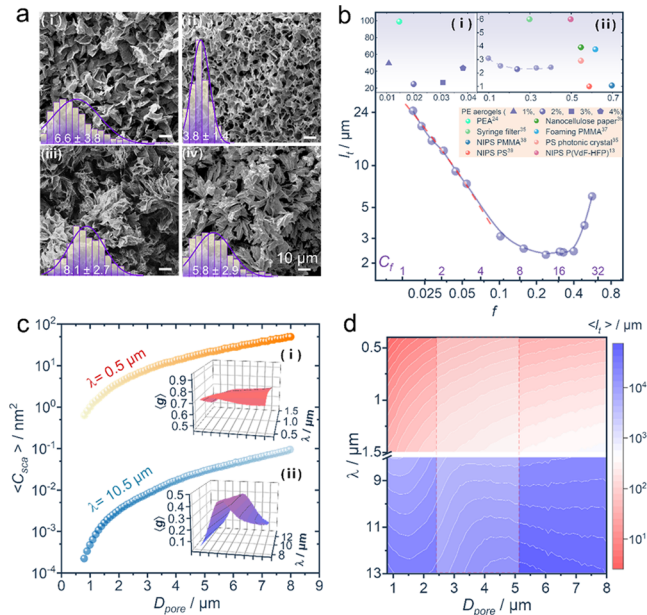


Figure 2. Structural optimization of PE aerogel. (a) SEM images of aerogels prepared from 1, 2, 3, and 4 wt % PE solutions (i–iv), respectively, with pore size distributions shown in the insets. (b) Transport mean free path l_t of PE aerogel under compression, with comparison among different structures shown in (a) (inset i) and other bright-white materials (insets i and ii). (c) Plot of the average scattering cross section ($\langle C_{\text{sca}} \rangle$) of an individual pore with different diameters; insets are the average scattering anisotropy ($\langle g \rangle$) in the vis-NIR (i) and MIR regions (ii), respectively. (d) Calculated l_t of pores with different diameters.

from loose (i), to dense (ii), and spherically aggregated nanoflake networks (iii, iv). Uniaxial compression (Figure S10 and Supporting Information, Note 4) was performed to investigate the scattering efficiency of different structures using the transport mean free path l_t as a figure of merit (calculated at 500 nm wavelength, see Supporting Information, Notes 5 and 6).

As can be seen in Figure 2b, for the PE aerogel prepared from 2 wt % solution (D_{pore} is $3.8 \pm 1.4 \mu\text{m}$, Figure 2a-ii), l_t decreases linearly at a low compression factor ($C_f \leq 5.1$, defined as the uncompressed/compressed thickness ratio) compatibly with a simple independent scattering interpretation. The shortest transport mean free path is reached at $C_f = 11.9$. At that point, the obtained PE aerogel appears as a flexible self-standing film with a remarkably low $l_t \sim 2.3 \mu\text{m}$. It is worth noting that the PE volume fraction f of this compressed aerogel is only 0.24, which is significantly lower than those of other artificial bright structures^{32,34–39} prepared from low-refractive-index materials (generally ranging from 1.48 to 1.6) (Figure 2b-i). At the same time, it is very close to the observed density of other optimally scattering structures^{33,34} including that of the white scales of *Cyphochilus* and *Lepidiota stigma* beetles,³⁴ which suggests that this value might represent an optimal density independent of the structure

morphology. In general, we found that all aerogels prepared from 1–4 wt % PE solutions achieve their lowest l_t when compressed by factors of 11–14 (Figure S12), with an absolute minimum reached by the 2 wt % sample due to its denser and highly disordered structure (Figure 2a-ii,b-i).

Serving as the cover layer on top of the emitter, there is a trade-off between the thickness of the aerogel and its scattering efficiency at different wavelengths (λ ; Supporting Information, Notes 6 and 7). Here, we have modeled the scattering properties of the aerogel by assuming a hollow sphere as the fundamental scattering unit to calculate its corresponding scattering cross section ($\langle C_{\text{sca}} \rangle$) over the visible and MIR spectrum (see Supporting Information, Note 8). As can be expected, $\langle C_{\text{sca}} \rangle$ is ~1000 times smaller at $10.5 \mu\text{m}$ than at $0.5 \mu\text{m}$ wavelength (Figure 2c), indicating the possibility to combine both high \bar{R}_{sun} and $\bar{\tau}_{\text{PE,MIR}}$ by modulating the pore size. Interestingly, a peak of the average scattering anisotropy (factor $\langle g \rangle$) is clearly visible around D_{pore} of $4 \mu\text{m}$ even after averaging over the experimentally determined polydisperse distribution of pore sizes (Figure 2c-ii), in good agreement with the pore diameter of $3.8 \pm 1.4 \mu\text{m}$ obtained for the best-performing aerogel prepared at 2 wt %. In this respect, controlling the pore size distribution allows to increase significantly the transport mean free path in the MIR region while leaving the scattering efficiency at visible wavelengths largely unaffected (Figure 2d).

Following the lamination of the aerogel with a commercial PDMS layer, we obtain a flexible bilayer PDRC film with a MIR emittance of ~0.8 (Figure 3a). The two layers show good adhesion with an estimated 90° peel strength exceeding 17 N m^{-1} (Supporting Information, Note 9). If needed, the adhesion strength and durability of the bilayer structure can be further improved by curing the prepolymer of PDMS directly on the aerogel surface.

Here, a PDMS film with a thickness of $150 \mu\text{m}$ was selected for its broad MIR emission, excellent flexibility, and higher heat conductivity (Supporting Information, Note 10).^{40–42} Recently, coatings have been reported to reduce the interface thermal resistance between the emitter and the substrate to cool,^{13,43} albeit increasing the costs for their removal and reuse. On the other hand, our bilayer PDRC film presents only moderate adhesion to substrates and can be therefore removed and/or reused in a sticker-like fashion to cool various materials including plastics, cements, and metals by 13 – 27°C (Figure 3b). Here, the reference temperature is taken in a region covered by bare PDMS films to exclude possible errors deriving from different emittance of substrates.

The cooling efficiency of the PE/PDMS bilayer film with $\bar{R}_{\text{sun}} = 0.960$ and $\bar{\tau}_{\text{PE,MIR}} = 0.788$ was measured in direct contact with external air (Figure 3c). Confronted with the adverse heat radiation from the surrounding high-rise buildings¹⁹ (Figure 3c, urban area in Beijing, 39.99°N , 116.32°E , altitude 58 m; continental monsoon climate), the bilayer film achieved a remarkable ΔT_{cool} of 5 – 6°C under intense I_{sun} exceeding 1000 W m^{-2} (Figure 3d), resulting in a measured cooling power (P_{cool}) of $70 \pm 14 \text{ W m}^{-2}$ (Figure 3e). In an open field with weaker I_{sun} (800 – 865 W m^{-2}) and lower relative humidity (RH, below 26%) (Turpan 42.95°N , 89.18°E , altitude 23 m; continental desert climate), we observed an increased ΔT_{cool} of 6 – 7°C (Figure 3f) and a P_{cool} of $78 \pm 12 \text{ W m}^{-2}$ (Figure 3g), which is still remarkable considering the low altitude, adverse air quality (PM10 of 74 and AQI of 63 in Sept 14; PM10 of 82 and AQI of 66 in Sept 16), and moderate insulation of the

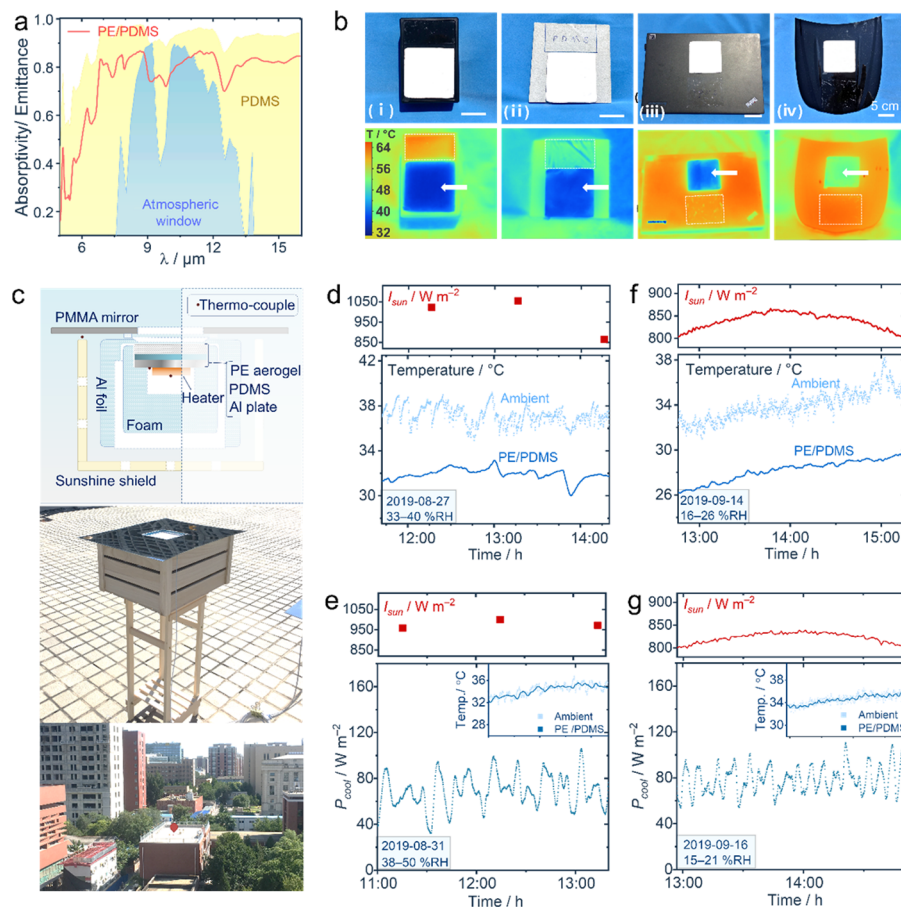


Figure 3. PDRC performance of PE/PDMS cooling skin. (a) MIR emission of PDMS before and after lamination with a 2.7 thick PE aerogel. (b) Thermal images of the bilayer PDRC film (pointed by the white arrow) on various surfaces, including plastic packaging, 64 °C (i), cement, 52 °C (ii), laptop computer, 60 °C (iii), and front cover of a car model, 62 °C (iv); dashed region was covered by bare PDMS film for reference purposes. (c) Schematic of the test equipment and environment in downtown Beijing. Sub-ambient temperature drops (ΔT_{cool} , (d) and (f)) and cooling powers (P_{cool} , (e) and (g)) respectively in downtown Beijing (d and e) and an open field in Turpan (f and g) with solar irradiance (I_{sun}) recorded; insets show temperatures of the ambient and the PE/PDMS layer.

equipment (we retrieved a heat transfer coefficient of $3 \text{ W m}^{-2} \text{ K}^{-1}$ fitted from the setup in Figure 3c, see Figure S19). Such service environments are generally far from the more idealized conditions under which many other PDRC experiments have been reported in the literature.^{12,13,24}

To investigate the cooperative effect between the radiative and nonradiative mechanisms on the PDRC performance, we compared the PDMS layer laminated with PE aerogels at different degrees of compressions C_f . During a gradual compression of the aerogel up to a factor of 8.6, \bar{R}_{sun} and $\bar{\tau}_{\text{PE,MIR}}$ are only slightly affected (Figure 4a-i), while thermal resistance (estimated by the ratio of thickness to thermal conductivity, t/k , Figure 4a-ii) is strongly reduced, determining an overall decreasing trend for the sub-ambient temperature, which is reproduced in the calculations ($\Delta T_{\text{cool,cal}}$; Figure 4a-iii and Supporting Information, Note 11). Although both $\Delta T_{\text{cool,cal}}$ and calculated cooling powers ($P_{\text{cool,cal}}$; Figure 4b) decline with increasing compression, thermal insulation always plays an active role by virtue of the considerably lower heat conductivity of PE aerogel compared to that of PDMS and other PDRC materials. Specifically, the enhanced thermal insulation of the PE aerogel cover can still overcome the adverse effects of weakened MIR emission of PDMS for values of $C_f < 3$, as determined by the intersection of $\Delta T_{\text{cool,cal}}$ at night when the influence of solar irradiation is absent (Figure 4b-

inset). At this threshold ($C_f = 3$), ΔT_{cool} is ~ 1.5 °C lower than that obtained using an uncompressed aerogel (Figure 4c).

Compared to the bare PDMS case, a 97.9% porosity PE aerogel efficiently inhibits the nonradiative heat transfer between PDMS and hot air, thereby increasing ΔT_{cool} by 1–2 °C at night (Figure 4d) and 9–13 °C at noontime (Figure 4e). Our theoretical modeling, which successfully reproduces the experimental data of Figures 3 and 4 and Supporting Information, Table 3, predicts a limiting cooling performance $\Delta T_{\text{cool}} \sim 14$ °C for a large-area PE/PDMS film (Figure S20, Supporting Information, Notes 11 and 12). It is worth noting that the PDMS emitter used alone cannot generate a net PDRC effect (Figure 4e), which highlights the true synergistic nature of our proposed approach. In principle, switching to a thicker aerogel layer with even higher porosity (we obtained samples up to 99.4% void fraction), holds promise to further improve the observed cooling performance. However, due to their lower scattering efficiency, these configurations require the presence of an additional solar reflector to compensate for the lower \bar{R}_{sun} ,²⁴ while the larger thicknesses might compromise $\bar{\tau}_{\text{PE,MIR}}$ leading to an overall lower ΔT_{cool} . Therefore, to extend traditional night-time cooling emitters (such as PDMS) to PDRC, it is paramount to fully optimize the structure of the front-side porous materials in terms of their scattering efficiency, which plays a key role in the delicate

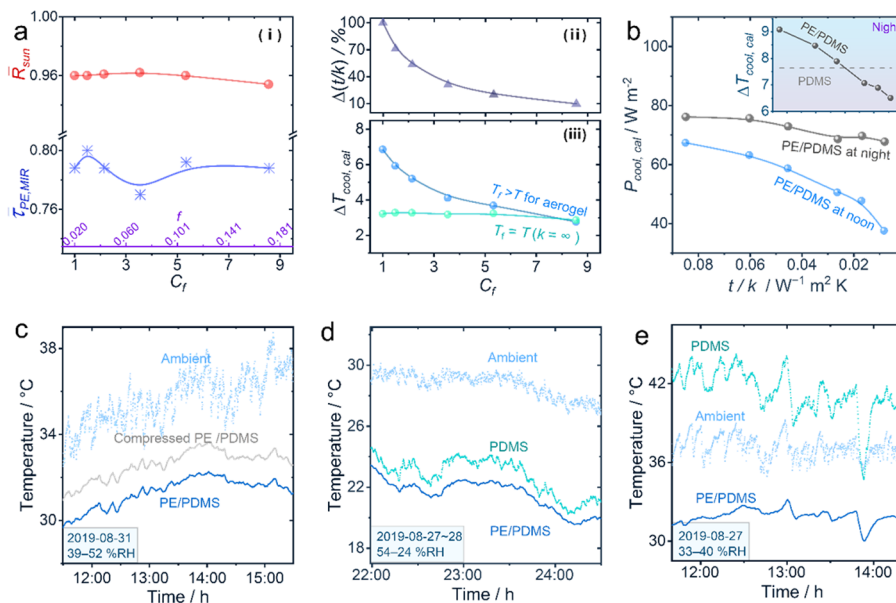


Figure 4. Cooperative effect between radiative and nonradiative mechanisms. (a) Simulated compression-dependent sub-ambient temperature drops ($\Delta T_{\text{cool},\text{cal}}$, a-iii)) using aerogel with \bar{R}_{sun} , $\tau_{\text{PE},\text{MIR}}$ (i) and thermal resistance (t/k , ii) change by compression, where T_f and T correspond to the temperature of the front and reverse sides of the aerogel, respectively. (b) Simulated cooling powers ($P_{\text{cool},\text{cal}}$) using aerogels with different t/k ; inset shows their $\Delta T_{\text{cool},\text{cal}}$ compared to that of bare PDMS at night. (c) ΔT_{cool} of bilayer PDRC films with PE aerogel before and after compression by a factor of 3. Cooling performance of PDMS covered with or without PE aerogel at (d) midnight and (e) noontime.

interplay among \bar{R}_{sun} , MIR transmittance, and thermal resistance. Moreover, thanks to the superhydrophobic characteristic of PE aerogels, dust can be easily rinsed off to maintain the long-term performance of the cooling bilayer (Supporting Information, Note 13).

CONCLUSIONS

In summary, we demonstrated a bioinspired bilayer route lowering the barriers to high-efficiency PDRC. A cooling skin integrating a flexible PE aerogel onto a simple PDMS film has been developed that can be easily applied and removed on various substrates repeatedly. A PE aerogel with 97.9% porosity was shown to effectively reflect sunlight while providing thermal insulation from external hot air. As a result, we demonstrated a ΔT_{cool} of 5–6 °C at noontime in a metropolitan environment, with a predicted cooling limit of 14 °C under ideal service conditions. Based on the optimized scattering efficiency of PE aerogel ($\bar{R}_{\text{sun}} \sim 0.96$, $\tau_{\text{PE},\text{MIR}} \sim 0.8$ for a 2.7 mm thick layer), the synergistic balance between radiative and nonradiative channels enables radiative cooling to reach its full potential, which is a key to expand the available range of materials for PDRC and their applications in real life. Since bright-white aerogels can be prepared from a wide array of materials (Supporting Information, Note 14), we expect that this method will inspire the exploration of different coatings with optimized scattering efficiency. In addition to passive cooling, bilayer devices for photothermal management are possibly available by changing the energy-conversion material, allowing for abundant applications in infrared stealth, solar-steam generation, and thermoelectric generation.^{8,44,45}

EXPERIMENTAL SECTION

Materials. Polyethylene (PE, $M_n \sim 4.5 \times 10^6$), cycloolefin copolymer (6013), and isotactic polypropylene ($M_w \sim 2 \times 10^6$) were supplied by Shanghai Lianle Chemical Industry Science and Technology Co. Ltd., Sinopec Beijing Research Institute of Chemical

Industry and Dalian University of Technology, respectively. PE of $M_w \sim 3.5 \times 10^4$ and poly(dimethylsiloxane) (PDMS) film were purchased from Sigma-Aldrich Co. LLC. and Hangzhou Bals Advanced Materials Co., Ltd., respectively. Paraffin wax (melting temperature of 48–50 °C), liquid paraffin, and cyclohexane were purchased from Sinopharm Chemical Reagent Beijing Co., Ltd. and used without purification. Antioxidant 1010 was purchased from Shanghai Aladdin Biochemical Technology Co., Ltd. Dispersion of multiwall carbon nanotubes was purchased from Nanjing XFNANO Materials Tech Co., Ltd. Orange acrylic paint was bought from MontMarte International Pty., Ltd.

Preparation of PE Aerogel. Typically, 1.5 g of PE powder ($M_n \sim 4.5 \times 10^6$), 73.5 g of paraffin (melting temperature of 48–50 °C), and 7.5 mg of antioxidant 1010 were stirred at 150 °C for 3 h. The resultant homogeneous solution was cast into a preheated mold and cooled by ice water (Figure S1). The as-formed gel was extracted with cyclohexane several times and freeze-dried. PE aerogels of different porosities were prepared in the same way but with varied PE concentrations (0.005–4 wt %). Diverse shapes of aerogel were achieved by casting in different molds, or by drafting or dip coating.

Preparation of Compressed Aerogels. The compression of aerogels was performed between two metal plates, as illustrated in Figure S2. Weighing paper was put between the metal plates and the samples before compression.

Adhesion of Aerogel and Poly(dimethylsiloxane). An aerogel slab was put on the surface of poly(dimethylsiloxane) film swelled by cyclohexane and then joined together by a negative pressure cavity due to the diffusion and volatilization of cyclohexane.

Characterizations. Morphological Characterization. The morphology of the samples was observed by field emission scanning electron microscope (JSM-7500F, JEOL, Japan).

Thermal Analysis. The infrared images were taken by the Fluke TiS65 infrared camera capturing infrared light of 7–14 μm wavelength, and the emittance and transmittance were set to be 0.95 and 1 in sequence before the measurements, respectively. The heat change of PE/paraffin solution during TIPS was monitored by differential scanning calorimetry (DSC Q2000, TA Instruments) at a cooling rate of 3 °C min⁻¹. The through-plane thermal conductivity of the compressed aerogels was measured on a laser-flash diffusivity instrument LFA 447 (NETZSCH, Germany). The specimens were cut into tablets with 0.2–2 mm thickness and spray-coated with a thin

graphite layer on both sides. The specific heat was detected by DSC Q2000 according to ISO 11357-4-2005. For the aerogels with a larger porosity (97.9–99.4%), their thermal conductivities are near the testing limits of the laser-flash method, so they were investigated by a Hot Disk 2500 s thermal constant analyzer based on transient plane sources.

Rheological Characterization. Mixture of 1 wt % PE/paraffin was fixed between two plates of 25 mm diameter and underwent temperature sweep by an ARES-G2 rotational rheometer (TA). The heating rate was 3 °C min⁻¹ at a strain of 1 Hz.

Dynamic Light Scattering Measurement. Dynamic light scattering investigation was performed on ALV/DLS/SLS-5022F (ALV-Laser Vertriebsgesellschaft m.b.H., Germany). Hot solutions of 0.5 wt % PE/paraffin and paraffin melt were filtered for dust removal before measurement. The structural variation in the liquids during cooling at 1.5 °C min⁻¹ was monitored with an incident angle at 45° and ethyl benzoate as the background liquid.

Observation of the TIPS Process. In situ observation of the TIPS of PE/paraffin solution (1 wt %) was performed using an optical microscope (BX51, Olympus, Japan) with a programmed thermostat. The cooling rate was 90 °C min⁻¹ (150–90 °C) and 30 °C min⁻¹ (90–40 °C) in sequence.

Mechanical Tests. Compression tests were performed on a UTM-16555 tensile tester (Shenzhen Suns Technology Stock Co., Ltd.). Cylindrical samples with diameters of ~20 mm and heights of ~25 mm were employed, and the strain rate was 10 mm min⁻¹.

Measurement of the Thickness of Nanoflakes. The specific surface area (A_s) was measured using Quantachrome NOVA 1200e and obtained from the adsorption curve by the BET method. The samples were degassed at 60 °C for 24 h prior to N₂ adsorption/desorption measurements at 77 K.

Reflectance/Transmittance Measurement. Total reflectance was measured in UV-vis-NIR (0.3–3 μm) and MIR (1–25 μm) ranges with integrating spheres. A UV-vis-NIR spectrometer (Lambda 950, Perkin Elmer, with a standard white diffuser (SRS-99-020, Labsphere) for the calibration) and Fourier transform infrared spectrometer (Vertex 70v, Bruker, with a gold integrating sphere (Model 4P-GPS-020-SL, Labsphere) and gold-coated Al foil as the reference) were used, respectively. Specular reflectance was determined by the difference of the total reflectance with and without opening the window at -8° axisymmetric to incident light direction in the UV-vis-NIR spectrometer. MIR transmittance was detected on the Vertex 70v spectrometer.

Angular-Resolved Measurement. A halogen lamp (HL2000, Ideaoptics, China) was fixed along the direction orthogonal to the film surface in a goniometer (R1, Ideaoptics, China). The detector (NOVA-EX, Ideaoptics, China) connected to a goniometer by a 600 μm core optic fiber (FIB-M-600-NIR, Ideaoptics, China) recorded the scattering light signal from 300 to 1000 nm wavelength at different angles subtending a solid angle of 3.9°. The light source was fixed at 0° and the detector was rotated from 90 to 270° in the transmittance mode. Integration time was adjusted from 1000 to 4000 ms depending on the thickness of the sample. Angular measurements were taken in steps of 5°.

Measurement of Refractive Index. Refractive index of the PE film was measured by a prism coupling meter (Model 2010, Metricon) using an incident light with the wavelength of 515.8, 637.7, and 1540 nm, respectively.

Efficiency of Radiative Cooling. Solar irradiance, humidity, and wind speed in the testing spots were obtained from the local weather bureau, or recorded in real time by CR-U8 weather station (Beijing Huachen Sunshine Technology Co., Ltd.), which is equipped with a SPN1 radiation meter, 034B wind direction and speed sensor, and CS215 temperature and humidity sensor. Temperatures were measured by the thermocouples (JY-DAM-PT08). The values of PM 2.5 and 10 were accessible on website (<https://www.aqistudy.cn>) and <http://www.cnemc.cn/>).

Sub-ambient temperature drop (ΔT_{cool}) of the aluminum plate covered by PDRC film was detected using the equipment shown in Figures 3c and S3, where the aluminum plate was the substrate to be

cooled, and the polystyrene foam was used to insulate the backside heat conduction and heat convection. Cooling power (P_{cool}) of PDRC film was approximately equal to the heating power to keep the temperature of the aluminum plate consistent with the room temperature.

Characterization of Surface Wettability. Static water contact angle was characterized using a drop shape analysis instrument (KRÜSS DSA 100, Germany) at ambient temperature. A water droplet of 5 μL was employed.

ASSOCIATED CONTENT

Supporting Information

The Supporting Information is available free of charge at <https://pubs.acs.org/doi/10.1021/acsami.0c03897>.

Experimental details; formation of the nanoflakes network; effects of molecular weights and PE concentration on the microstructure of aerogel; mechanical performance and microstructure under compression; dependence of specular reflection on compression factor; calculations of the transport mean free path (l_t); l_t of different aerogels; solar reflectance of aerogels; effects of thickness on the MIR reflectance; simulations on the scattering performance of pores of different sizes; peeling tests of PE aerogel layer and PDMS layer; cooling performance for MIR emitter of different thermal conductivity; simulations of PDRC performance; cooling performance in different weather conditions; superhydrophobicity and self-cleaning; and universality of TIPS method to prepare nanoflake aerogels ([PDF](#))

AUTHOR INFORMATION

Corresponding Authors

Ning Zhao – Beijing National Laboratory for Molecular Sciences, CAS Research/Education Center for Excellence in Molecular Sciences, Laboratory of Polymer Physics and Chemistry, Institute of Chemistry, Chinese Academy of Sciences, Beijing 100190, P. R. China; University of Chinese Academy of Sciences, Beijing 100049, P. R. China; orcid.org/0000-0002-3569-3850; Phone: +86-010-82619667; Email: zhaoning@iccas.ac.cn

Lorenzo Pattelli – European Laboratory for Non-Linear Spectroscopy (LENS), Università di Firenze, Sesto Fiorentino, FI 50019, Italy; Istituto Nazionale di Ricerca Metrologica (INRIM), Turin 10135, Italy; Phone: +39-055-4572477; Email: l.pattelli@inrim.it

Jian Xu – Shenzhen University, Shenzhen 518061, P. R. China; orcid.org/0000-0002-9370-4829; Phone: +86-010-82619667; Email: jxu@iccas.ac.cn

Authors

Meng Yang – Beijing National Laboratory for Molecular Sciences, CAS Research/Education Center for Excellence in Molecular Sciences, Laboratory of Polymer Physics and Chemistry, Institute of Chemistry, Chinese Academy of Sciences, Beijing 100190, P. R. China; University of Chinese Academy of Sciences, Beijing 100049, P. R. China

Weizhi Zou – Beijing National Laboratory for Molecular Sciences, CAS Research/Education Center for Excellence in Molecular Sciences, Laboratory of Polymer Physics and Chemistry, Institute of Chemistry, Chinese Academy of Sciences, Beijing 100190, P. R. China; University of Chinese Academy of Sciences, Beijing 100049, P. R. China

Jing Guo — Beijing National Laboratory for Molecular Sciences, CAS Research/Education Center for Excellence in Molecular Sciences, Laboratory of Polymer Physics and Chemistry, Institute of Chemistry, Chinese Academy of Sciences, Beijing 100190, P. R. China; University of Chinese Academy of Sciences, Beijing 100049, P. R. China

Zhenchao Qian — Beijing National Laboratory for Molecular Sciences, CAS Research/Education Center for Excellence in Molecular Sciences, Laboratory of Polymer Physics and Chemistry, Institute of Chemistry, Chinese Academy of Sciences, Beijing 100190, P. R. China; University of Chinese Academy of Sciences, Beijing 100049, P. R. China

Heng Luo — Beijing National Laboratory for Molecular Sciences, CAS Research/Education Center for Excellence in Molecular Sciences, Laboratory of Polymer Physics and Chemistry, Institute of Chemistry, Chinese Academy of Sciences, Beijing 100190, P. R. China; University of Chinese Academy of Sciences, Beijing 100049, P. R. China

Shijia Yang — Beijing National Laboratory for Molecular Sciences, CAS Research/Education Center for Excellence in Molecular Sciences, Laboratory of Polymer Physics and Chemistry, Institute of Chemistry, Chinese Academy of Sciences, Beijing 100190, P. R. China; University of Chinese Academy of Sciences, Beijing 100049, P. R. China

Diederik S. Wiersma — European Laboratory for Non-Linear Spectroscopy (LENS), Università di Firenze, Sesto Fiorentino, FI 50019, Italy; Istituto Nazionale di Ricerca Metrologica (INRIM), Turin 10135, Italy

Complete contact information is available at:

<https://pubs.acs.org/10.1021/acsami.0c03897>

Notes

The authors declare no competing financial interest.

ACKNOWLEDGMENTS

The authors would like to acknowledge financial support from the Chinese Academy of Sciences (No. QYZDB-SSW-SLH025) and National Natural Science Foundation of China (51673203 and 51522308).

REFERENCES

- (1) Lesk, C.; Rowhani, P.; Ramankutty, N. Influence of Extreme Weather Disasters on Global Crop Production. *Nature* **2016**, *529*, 84–98.
- (2) Panteli, M.; Mancarella, P. Influence of Extreme Weather and Climate Change on the Resilience of Power Systems: Impacts and Possible Mitigation Strategies. *Electr. Power Syst. Res.* **2015**, *127*, 259–270.
- (3) Cai, L.; Song, A. Y.; Li, W.; Hsu, P.-C.; Lin, D.; Catrysse, P. B.; Liu, Y.; Peng, Y.; Chen, J.; Wang, H.; Xu, J.; Yang, A.; Fan, S.; Cui, Y. Spectrally Selective Nanocomposite Textile for Outdoor Personal Cooling. *Adv. Mater.* **2018**, *30*, No. 1802152.
- (4) Tao, P.; Shang, W.; Song, C.; Shen, Q.; Zhang, F.; Luo, Z.; Yi, N.; Zhang, D.; Deng, T. Bioinspired Engineering of Thermal Materials. *Adv. Mater.* **2015**, *27*, 428–463.
- (5) Schroeder, T. B. H.; Houghtaling, J.; Wilts, B. D.; Mayer, M. It's not a bug, it's a Feature: Functional Materials in Insects. *Adv. Mater.* **2018**, *30*, No. 1705322.
- (6) Shi, N. N.; Tsai, C.-C.; Canimo, F.; Bernard, G. D.; Yu, N.; Wehner, N. Keeping Cool: Enhanced Optical Reflection and Radiative Heat Dissipation in Saharan Silver Ants. *Science* **2015**, *349*, 298–301.
- (7) Zhou, H.; Xu, J.; Liu, X.; Zhang, H.; Wang, D.; Chen, C.; Zhang, D.; Fan, T. Bio-Inspired Photonic Materials: Prototypes and Structural Effect Designs for Applications in Solar Energy Manipulation. *Adv. Funct. Mater.* **2018**, *28*, No. 1705309.
- (8) Du, A.; Wang, H.; Zhou, B.; Zhang, C.; Wu, X.; Ge, Y.; Niu, T.; Ji, X.; Zhang, T.; Zhang, Z.; Wu, G.; Shen, J. Multifunctional Silica Nanotube Aerogels Inspired by Polar Bear Hair for Light Management and Thermal Insulation. *Chem. Mater.* **2018**, *30*, 6849–6857.
- (9) Cui, Y.; Gong, H.; Wang, Y.; Li, D.; Bai, H. A Thermally Insulating Textile Inspired by Polar Bear Hair. *Adv. Mater.* **2018**, *30*, No. 1706807.
- (10) Stegmaier, T.; Linke, M.; Planck, H. Bionics in Textiles: Flexible and Translucent Thermal Insulations for Solar Thermal Applications. *Philos. Trans. R. Soc., A* **2009**, *367*, 1749–1758.
- (11) Munday, J. N. Tackling Climate Change Through Radiative Cooling. *Joule* **2019**, *3*, 2057–2060.
- (12) Li, T.; Zhai, Y.; He, S.; Gan, W.; Wei, Z.; Heidarnejad, M.; Dalgo, D.; Mi, R.; Zhao, X.; Song, J.; Dai, J.; Chen, C.; Aili, A.; Vellore, A.; Martini, A.; Yang, R.; Srebric, J.; Yin, X.; Hu, L. A Radiative Cooling Structural Material. *Science* **2019**, *364*, 760–763.
- (13) Mandal, J.; Fu, Y.; Overvig, A.; Jia, M.; Sun, K.; Shi, N.; Zhou, H.; Xiao, X.; Yu, N.; Yang, Y. Hierarchically Porous Polymer Coatings for Highly Efficient Passive Daytime Radiative Cooling. *Science* **2018**, *362*, 315–318.
- (14) Raman, A. P.; Anoma, M. A.; Zhu, L.; Rephaeli, E.; Fan, S. Passive Radiative Cooling below Ambient Air Temperature under Direct Sunlight. *Nature* **2014**, *515*, 540–544.
- (15) Wang, X.; Liu, X.; Li, Z.; Zhang, H.; Yang, Z.; Zhou, H.; Fan, T. Scalable Flexible Hybrid Membranes with Photonic Structures for Daytime Radiative Cooling. *Adv. Funct. Mater.* **2019**, *30*, No. 1907562.
- (16) Zeyghami, M.; Goswami, D. Y.; Stefanakos, E. A Review of Clear Sky Radiative Cooling Developments and Applications in Renewable Power Systems and Passive Building Cooling. *Sol. Energy Mater. Sol. Cells* **2018**, *178*, 115–128.
- (17) Zhao, B.; Hu, M.; Ao, X.; Chen, N.; Pei, G. Radiative Cooling: A Review of Fundamentals, Materials, Applications, and Prospects. *Appl. Energy* **2019**, *236*, 489–513.
- (18) Zhai, Y.; Ma, Y.; David, S. N.; Zhao, D.; Lou, R.; Tan, G.; Yang, R.; Yin, X. Scalable-Manufactured Randomized Glass-Polymer Hybrid Metamaterial for Daytime Radiative Cooling. *Science* **2017**, *355*, 1062–1066.
- (19) Zhou, L.; Song, H.; Liang, J.; Singer, M.; Zhou, M.; Stegenburgs, E.; Zhang, N.; Xu, C.; Ng, T.; Yu, Z.; Ooi, C.; Gan, Q. A Polydimethylsiloxane-Coated Metal Structure for All-Day Radiative Cooling. *Nat. Sustainability* **2019**, *2*, 718–724.
- (20) Bhatia, B.; Leroy, A.; Shen, Y.; Zhao, L.; Gianello, M.; Li, D.; Gu, T.; Hu, J.; Soljačić, M.; Wang, E. N. Passive Directional Sub-Ambient Daytime Radiative Cooling. *Nat. Commun.* **2018**, *9*, No. 5001.
- (21) Zhao, B.; Hu, M.; Ao, X.; Pei, G. Performance Evaluation of Daytime Radiative Cooling under Different Clear Sky Conditions. *Appl. Therm. Eng.* **2019**, *155*, 660–666.
- (22) Liu, X.; Iocozzia, J.; Wang, Y.; Cui, X.; Chen, Y.; Zhao, S.; Li, Z.; Lin, Z. Noble Metal-Metal Oxide Nanostructures with Tailored Nanostructures for Efficient Solar Energy Conversion, Photocatalysis and Environmental Remediation. *Energy Environ. Sci.* **2017**, *10*, 402–434.
- (23) Kim, H.; Lenert, A. Optical and Thermal Filtering Nanoporous Materials for Sub-Ambient Radiative Cooling. *J. Opt.* **2018**, *20*, No. 084002.
- (24) Leroy, A.; Bhatia, B.; Kelsall, C. C.; Castillejo-Cuberos, A.; Di Capua, H. M.; Zhao, L.; Zhang, L.; Guzman, A. M.; Wang, E. N. High-Performance Subambient Radiative Cooling Enabled by Optically Selective and Thermally Insulating Polyethylene Aerogel. *Sci. Adv.* **2019**, *5*, No. eaat9480.
- (25) Peng, Y.; Chen, J.; Song, A. Y.; Catrysse, P. B.; Hsu, P.-C.; Cai, L.; Liu, B.; Zhu, Y.; Zhou, G.; Wu, D. S.; Lee, H. R.; Fan, S.; Cui, Y. Nanoporous Polyethylene Microfibres for Large-Scale Radiative Cooling Fabric. *Nat. Sustainability* **2018**, *1*, 105–112.

- (26) Fu, Y.; Yang, J.; Su, Y. S.; Du, W.; Ma, Y. G. Daytime Passive Radiative Cooler Using Porous Alumina. *Sol. Energy Mater. Sol. Cells* **2019**, *191*, 50–54.
- (27) Li, N.; Wang, J.; Liu, D.; Huang, X.; Xu, Z.; Zhang, C.; Zhang, Z.; Zhong, M. Selective Spectral Optical Properties and Structure of Aluminum Phosphate for Daytime Passive Radiative Cooling Application. *Sol. Energy Mater. Sol. Cells* **2019**, *194*, 103–110.
- (28) Lavoine, N.; Bergstrom, L. Nanocellulose-Based Foams and Aerogels: Processing, Properties, and Applications. *J. Mater. Chem. A* **2017**, *5*, 16105–16117.
- (29) Qiu, L.; He, Z.; Li, D. Multifunctional Cellular Materials Based on 2D Nanomaterials: Prospects and Challenges. *Adv. Mater.* **2018**, *30*, No. 1704850.
- (30) Tanaka, H.; Araki, T. Phase Inversion During Viscoelastic Phase Separation: Roles of Bulk and Shear Relaxation Moduli. *Phys. Rev. Lett.* **1997**, *78*, 4966–4969.
- (31) Zhang, J. N.; Zhang, Z. L.; Zhang, H. D.; Yang, Y. L. Kinetics and Morphologies of Viscoelastic Phase Separation. *Phys. Rev. E* **2001**, *64*, No. 051510.
- (32) Luke, S. M.; Hallam, B. T.; Vukusic, P. Structural Optimization for Broadband Scattering in Several Ultra-Thin White Beetle Scales. *Appl. Opt.* **2010**, *49*, 4246–4254.
- (33) Pattelli, L.; Egel, A.; Lemmer, U.; Wiersma, D. S. Role of Packing Density and Spatial Correlations in Strongly Scattering 3D Systems. *Optica* **2018**, *5*, 1037–1045.
- (34) Burg, S. L.; Washington, A.; Coles, D. M.; Bianco, A.; McLoughlin, D.; Mykhaylyk, O. O.; Villanova, J.; Dennison, A. J. C.; Hill, C. J.; Vukusic, P.; Doak, S.; Martin, S. J.; Hutchings, M.; Parnell, S. R.; Vasilev, C.; Clarke, N.; Ryan, A. J.; Furnass, W.; Croucher, M.; Dalgliesh, R. M.; Prevost, S.; Dattani, R.; Parker, A.; Jones, R. A. L.; Fairclough, J. P. A.; Parnell, A. J. Liquid–Liquid Phase Separation Morphologies in Ultra-White Beetle Scales and a Synthetic Equivalent. *Commun. Chem.* **2019**, *2*, No. 100.
- (35) Burresi, M.; Cortese, L.; Pattelli, L.; Kolle, M.; Vukusic, P.; Wiersma, D. S.; Steiner, U.; Vignolini, S. Bright-White Beetle Scales Optimise Multiple Scattering of Light. *Sci. Rep.* **2015**, *4*, No. 6075.
- (36) Caixeiro, S.; Peruzzo, M.; Onelli, O. D.; Vignolini, S.; Sapienza, R. Disordered Cellulose-Based Nanostructures for Enhanced Light Scattering. *ACS Appl. Mater. Interfaces* **2017**, *9*, 7885–7890.
- (37) Syurik, J.; Siddique, R. H.; Dollmann, A.; Gomard, G.; Schneider, M.; Worgull, M.; Wiegand, G.; Hölscher, H. Bio-Inspired, Large Scale, Highly-Scattering Films for Nanoparticle-Alternative White Surfaces. *Sci. Rep.* **2017**, *7*, No. 46637.
- (38) Syurik, J.; Jacucci, G.; Onelli, O. D.; Hoelscher, H.; Vignolini, S. Bio-Inspired Highly Scattering Networks via Polymer Phase Separation. *Adv. Funct. Mater.* **2018**, *28*, No. 1706901.
- (39) Zou, W.; Pattelli, L.; Guo, J.; Yang, S.; Yang, M.; Zhao, N.; Xu, J.; Wiersma, S. Biomimetic Polymer Film with Brilliant Brightness Using a One-Step Water Vapor-Induced Phase Separation Method. *Adv. Funct. Mater.* **2019**, *29*, No. 1808885.
- (40) Kou, J.; Jurado, Z.; Chen, Z.; Fan, S.; Minnich, A. J. Daytime Radiative Cooling Using Near-Black Infrared Emitters. *ACS Photonics* **2017**, *4*, 626–630.
- (41) Lötters, J. C.; Olthuis, W.; Veltink, P. H.; Bergveld, P. The Mechanical Properties of the Rubber Elastic Polymer Polydimethylsiloxane for Sensor Applications. *J. Micromech. Microeng.* **1997**, *7*, 145–147.
- (42) Yang, S.; Khare, K.; Lin, P.-C. Harnessing Surface Wrinkle Patterns in Soft Matter. *Adv. Funct. Mater.* **2010**, *20*, 2550–2564.
- (43) Choi, S. H.; Kim, S.-W.; Ku, Z.; Visbal-Onufra, M. A.; Kim, S.-R.; Choi, K.-H.; Ko, H.; Choi, W.; Urbas, A. M.; Goo, T.-W.; Kim, Y.-L. Anderson Light Localization in Biological Nanostructures of Native Silk. *Nat. Commun.* **2018**, *9*, No. 452.
- (44) Ke, Y.; Chen, J.; Lin, C.; Wang, S.; Zhou, Y.; Yin, J.; Lee, P. S.; Long, Y. Smart Windows: Electro-, Thermo-, Mechano-, Photochromics, and Beyond. *Adv. Energy Mater.* **2019**, *9*, No. 1902066.
- (45) Hu, X.; Zhu, J. Tailoring Aerogels and Related 3D Macroporous Monoliths for Interfacial Solar Vapor Generation. *Adv. Funct. Mater.* **2019**, *30*, No. 1907234.